clean technologies

MDPI

Article

Solvothermal Synthesis and Carbon Capture Performance of Terephthalate-Linked $Zn_{0.75}Mg_{0.25}$ MOF-74: Effects of Synthesis Conditions on Structure and CO_2 Adsorption

Siyabonga Brighton Ndebele [1], Glory Makuwa [1], Djemima Bulanga [1], Thembelihle Masombuka [1,2] and Major Mabuza [1,*]

[1] Department of Chemical Engineering Technology, University of Johannesburg, Doornfontein, Johannesburg 2088, South Africa; siyabongandebele13@gmail.com (S.B.N.); glorymakuwa1@gmail.com (G.M.); djemimabl@gmail.com (D.B.); tmehlo@csir.co.za (T.M.)
[2] HySA and CCU, Centre for Nanostructures and Advanced Materials (CeNAM), Chemicals Cluster, Council for Scientific and Industrial Research (CSIR), Pretoria 0001, South Africa
* Correspondence: majorm@uj.ac.za; Tel.: +27-11-559-6402

Abstract

Coal-fired power generation remains a major source of carbon dioxide (CO_2) emissions, and metal–organic framework-74 (MOF-74) materials offer high adsorption capacity but rely on costly 2,5-dihydroxyterephthalic acid linkers that limit scalability. This study synthesized bimetallic $Zn_{0.75}Mg_{0.25}$-MOF-74 using terephthalic acid (TPA) as a cheaper alternative linker and evaluated the effect of synthesis reaction temperature (89–160 °C) and time (5–55.5 h) on its physicochemical properties for carbon capture. Samples were prepared solvothermally and characterized by FTIR, XRD, SEM-EDS, and N_2 (77 K) and CO_2 (293 K) adsorption analysis. FTIR confirmed metal–ligand coordination; XRD verified crystalline MOF-74 formation, and SEM showed well-defined rod-like morphology at 100 °C, 12 h and 125 °C, 30 h. Direct CO_2 adsorption on the 125 °C, 30 h sample yielded a Type I isotherm characteristic of micropore filling, with an uptake of 0.31 mmol/g at ~1 bar and 0.072 mmol/g at flue-gas-relevant conditions (~0.135 bar). Its CO_2-derived BET surface area (60.10 m^2/g) and Dubinin–Astakhov micropore area (131.69 m^2/g) far exceeded N_2-derived values, confirming ultra-micropores accessible to CO_2 but not to N_2 at 77 K. TPA therefore yields a stable, microporous CO_2-adsorbing framework, trading some capacity for lower cost and scalability. Future investigations should systematically evaluate long-term cycling stability and adsorption performance under mixed-gas operating conditions.

Keywords: bimetallic MOF-74; carbon capture; CO_2 adsorption; solvothermal synthesis; microporosity; terephthalic acid; Zn/Mg-MOF-74

Check for updates

Academic Editor: Giuseppina Vanga

Received: 21 July 2026
Revised: 1 September 2026
Accepted: 8 September 2026
Published: 11 September 2026

Copyright: © 2026 by the authors. Licensee MDPI, Basel, Switzerland. This article is an open access article distributed under the terms and conditions of the Creative Commons Attribution (CC BY) license.

1. Introduction

Mitigating carbon dioxide (CO_2) emissions from large-scale energy production remains central to achieving global climate stability and sustainable industrial progress [1]. Coal-fired power plants supply approximately 35% of global electricity demand while contributing 30–40% of CO_2 emissions from fossil fuel combustion, making them both a dominant energy source and a major emitter [2,3]. South Africa is particularly exposed, with coal accounting for approximately 89% of electricity generation and the country ranking as the 15th highest per capita CO_2 emitter globally in 2022 [4,5]. This reliance accelerates

climate change and contributes to atmospheric pollution, thereby increasing the unforeseen human respiratory-related diseases [6]. Addressing CO_2 emissions from coal-fired plants is therefore essential to limiting both global and local environmental impacts while supporting a transition to more sustainable energy production [1].

Each of the existing capture technologies carry significant shortcomings. Amine-based chemical absorption, though widely deployed, suffers from high regeneration costs and corrosion [7], while cryogenic separation demands prohibitive energy input at scale [8]. Adsorption on hydrophilic solids such as zeolites is inefficient in humid conditions, as water molecules adsorb preferentially and saturate the active sites [9]. Activated carbon is affordable but exhibits poor CO_2 selectivity under industrial flue-gas conditions, which are typically 25–75 °C, 0.1–1 bar, and 10–15% CO_2 alongside N_2, O_2, and up to 20% moisture [10,11].

CO_2 management spans capture, utilization, and storage, and the route chosen sets the requirements on the adsorbent. Post-combustion capture treats dilute flue gas at near-ambient pressure and is the option most readily retrofitted to existing coal plants [6]. Pre-combustion capture works on shifted syngas at elevated pressure and higher CO_2 concentration, which favours physisorbents with high working capacity. Oxy-fuel combustion avoids separation altogether by burning in oxygen at the cost of an air separation unit. Beyond capture, conversion routes such as cycloaddition to cyclic carbonates treat CO_2 as a feedstock rather than a waste [12]. MOFs are of interest across both domains since the open metal sites that bind CO_2 also activate it towards reaction, and Zn/Mg-MOF-74 has been applied to cyclic carbonate formation as well as adsorption [13]. A low-cost MOF-74 analogue is therefore of interest for more than capture alone.

Metal–organic frameworks (MOFs), crystalline porous materials formed from metal nodes bridged by organic linkers, have emerged as promising carbon capture alternatives due to their high surface area, tuneable porosity, and chemical versatility [14]. The MOF-74 is distinguished by a one-dimensional hexagonal channel structure with a high density of open metal sites, whose exposed metal centres interact strongly with gas molecules and make the framework particularly effective for CO_2 capture and separation [15,16]. Compared with these conventional adsorbents, the case for MOF-74 rests less on raw surface area than on the nature of the adsorption site itself. The contrast between the two benchmarks is instructive: zeolite 13X adsorbs 95.80 mg/g (2.18 mmol/g) of CO_2 from a 10% CO_2 stream at 303 K and 1 atm on a BET surface area of only 472 m^2/g [17], whereas a coconut-shell activated carbon with almost three times that surface area, 1378 m^2/g, takes up just 1.86 mmol/g under comparable dynamic conditions [18]. Surface area alone therefore predicts neither capacity nor suitability. What separates them is the adsorption mechanism, and each mechanism carries its own liability under real flue gas: the cationic sites that make zeolite 13X an effective CO_2 adsorbent are the same sites at which water adsorbs preferentially [9], while the non-specific pore filling that makes activated carbon humidity-tolerant leaves it unable to discriminate CO_2 from N_2 at flue-gas partial pressures [10,11].

MOF-74 resolves this trade-off differently, and more consequentially, it leaves the resolution open to adjustment. Its coordinatively unsaturated metal centres bind CO_2 directly through Lewis acid–base interaction, producing appreciable uptake at the low partial pressures where non-specific physisorbents fail [15,16]. Those centres are also substitutional: the same hexagonal channel topology is retained across Mg^{2+}, Zn^{2+}, Ni^{2+}, and Co^{2+} variants, so CO_2 binding strength can be shifted systematically through the choice of metal without altering the framework architecture [19]. Adsorption capacity, regeneration energy, and hydrothermal stability therefore become design variables rather than fixed properties of a given adsorbent, which is a degree of control that neither zeolites

nor activated carbons afford and the basis on which the bimetallic frameworks considered below are constructed.

The choice of metal centre imposes a clear trade-off between capacity and stability. In Zn-MOF-74, exposed Zn^{2+} centres bind CO_2 electrostatically, but a moderate binding energy of 20–30 kJ/mol limits retention at low partial pressures, and CO_2 uptake reaches only 4–5 mmol/g at 1 bar and 298 K [20–22]. Its isostructural counterpart Mg-MOF-74 achieves a superior uptake of approximately 8 mmol/g under the same conditions, as the smaller ionic radius and higher charge density of Mg^{2+} drive stronger Lewis acid–base interactions [19,23]; this comes at the cost of a higher regeneration energy of 35–40 kJ/mol and extreme moisture sensitivity since hydrolysis of Mg-O bonds causes rapid structural collapse in humid environments [19,21,24]. Bimetallic Zn/Mg-MOF-74 presents a potential solution to overcome the shortcomings of the monometallic MOF-74 variants. Incorporating Zn^{2+} improves hydrothermal stability, as Zn-O bonds resist hydrolysis, while retaining Mg^{2+} preserves high CO_2 uptake at low partial pressures [12,13]. The resulting intermediate binding energy of 25–35 kJ/mol balances adsorption capacity against regeneration efficiency [25].

Solvothermal synthesis is preferred for these frameworks, as dissolving metal precursors and organic linkers under elevated temperature and pressure promotes slow, uniform crystallization and yields high-purity, well-crystallized products with controlled morphology and porosity [13,26]. Mechanochemical, microwave-assisted and hydrothermal routes, by contrast, frequently produce incomplete reactions, uneven crystallization, or hydrolysis-related instability arising from poor linker solubility [20,21,27]. Even so, industrial deployment of MOF-74 remains constrained by framework stability, moisture sensitivity, and above all the cost of the 2,5-dihydroxyterephthalic acid (2,5-DHTP) linker [28,29].

Terephthalic acid (TPA) offers a cost-effective alternative, combining wide commercial availability with competitive pricing, which makes it an attractive option for reducing the overall production cost while maintaining the desired product quality. Reported syntheses of Zn/Mg-MOF-74 have relied exclusively on 2,5-DHTP, whose hydroxyl (-OH) and carboxyl (-COOH) groups both coordinate to metal ions, forming the strong metal–oxygen bonds that stabilize the characteristic open-metal-site structure [20]. Those -OH groups raise framework polarity and CO_2 affinity, but they also render MOF-74 strongly hydrophilic, allowing water to compete with CO_2 for open metal sites and promoting hydrolysis of metal–oxygen bonds in humid environments [30,31]. The 2,5-DHTP costs approximately USD 299.10 per 5 g against USD 48.72 per 25 g for TPA, assessed to be six times more per unit mass, and its reactive hydroxyl groups and multi-step synthesis make it highly sensitive to variations in solvent, pH, and temperature [32,33]. TPA is an inexpensive, widely available aromatic dicarboxylic acid that still forms stable coordination networks with Zn^{2+} and Mg^{2+} through its carboxylate oxygens, while its rigid planar benzene backbone supports uniform pore structures and high thermal stability comparable to robust frameworks such as MIL-53 and UiO-66 [34–36]. TPA is less polar but more thermally and moisture-stable than 2,5-DHTP, though it lacks hydroxyl groups [37].

Reported syntheses of bimetallic Zn/Mg-MOF-74 have relied exclusively on 2,5-DHTP, and the framework has not previously been reported with a linker lacking hydroxyl coordination sites. This study addresses that gap. It evaluated the feasibility of synthesizing bimetallic $Zn_{0.75}Mg_{0.25}$-MOF-74 using TPA as a proxy for 2,5-DHTP and determined how synthesis reaction temperature (89–160 °C) and time (5–55.5 h) affect crystallinity, morphology, surface area, pore structure, and CO_2 adsorption performance. Establishing that a functional framework forms on a linker six times cheaper per unit mass is a precondition for scaling MOF-74 towards post-combustion capture, and the results define the processing window within which it does. Materials were prepared solvothermally and character-

ized by Fourier Transform Infrared (FTIR), X-ray diffraction (XRD), Scanning Electron Microscopy paired with Energy-Dispersive X-ray (SEM-EDS), and gas adsorption analysis.

2. Materials and Methods

2.1. Materials

Zinc nitrate hexahydrate (98%), magnesium nitrate hexahydrate (98%), and terephthalic acid (98%) were supplied by Protea Laboratory Solutions (Pty) Ltd (Midrand, South Africa). N,N-dimethylformamide (99.98%), ethanol (98%), and methanol (98%) were supplied by Axiom Chemlab Supplies (Pty) Ltd (Midrand, South Africa). Deionized water was obtained from the University of Johannesburg laboratory, and Teflon-lined stainless-steel autoclaves were supplied by Glassworld (Johannesburg, South Africa). All reagents were of analytical grade and were used as received without further purification.

2.2. Synthesis of Bimetallic Zn/Mg-MOF-74

The synthesis of the bimetallic Zn/Mg-MOF-74 was conducted using a solvothermal method adapted from Gao et al. [13], with variations in reaction temperature, time, and the use of terephthalic acid (TPA) as an alternative linker to 2,5-dihydroxyterephthalic acid. The outcomes of the study by Gao et al. [13] showed that the $Zn_{0.75}Mg_{0.25}$-MOF-74 ratio had the best CO_2 adsorption performance; therefore, that was the MOF ratio that was synthesized in this study. The procedure involved dissolving 6 g zinc nitrate hexahydrate and 1.258 g magnesium nitrate hexahydrate in an already mixed solution of 0.946 g TPA, 450 mL N,N-dimethylformamide (DMF), 30 mL ethanol, and 30 mL deionized water. The initial solution was mixed for 10 min at a speed of 400 rpm at room temperature. Zinc nitrate hexahydrate and magnesium nitrate hexahydrate were then added to the solution and stirred for a further 10 min at the same mixing conditions until the solution was transparent with no visible precipitates. The homogeneous solution was then distributed in equal amounts into three 250 mL Teflon-lined stainless-steel autoclaves, which were subsequently transferred to an oven as shown in Figure 1, where they were heated at controlled temperatures and time conditions to promote gradual crystal formation and uniform metal distribution.

A Design-Expert-13 central composite design with 2 input factors was used as an experimental design to evaluate the effects of synthesis temperature (100–150 °C) and reaction time (12–48 h) on framework structural integrity, morphology, functional groups, and textural properties. Design-Expert-13 generated axial points beyond the factorial ranges to validate the data, adding temperatures of 89 °C and 160 °C and reaction times of 5 h and 55.5 h, with 125 °C and 30 h as the centre point. The input parameters were selected based on literature evidence that optimal solvothermal conditions around 125 °C for 30 h yield well-defined MOF-74 structures with high CO_2 uptake [13].

After the solvothermal reaction, the autoclaves were retrieved from the oven and cooled to room temperature by soaking in cool water to gently stop the synthesis process. The resulting white product was recovered by manual decanting. A multi-stage purification process followed, consisting of washing twice with methanol using a centrifuge at 4000 rpm for 10 min and soaking for 6 h to remove unreacted precursors and organic residues. The purified crystals were oven-dried at 110 °C for 12 h, yielding a white powder as shown in Figure 1f.

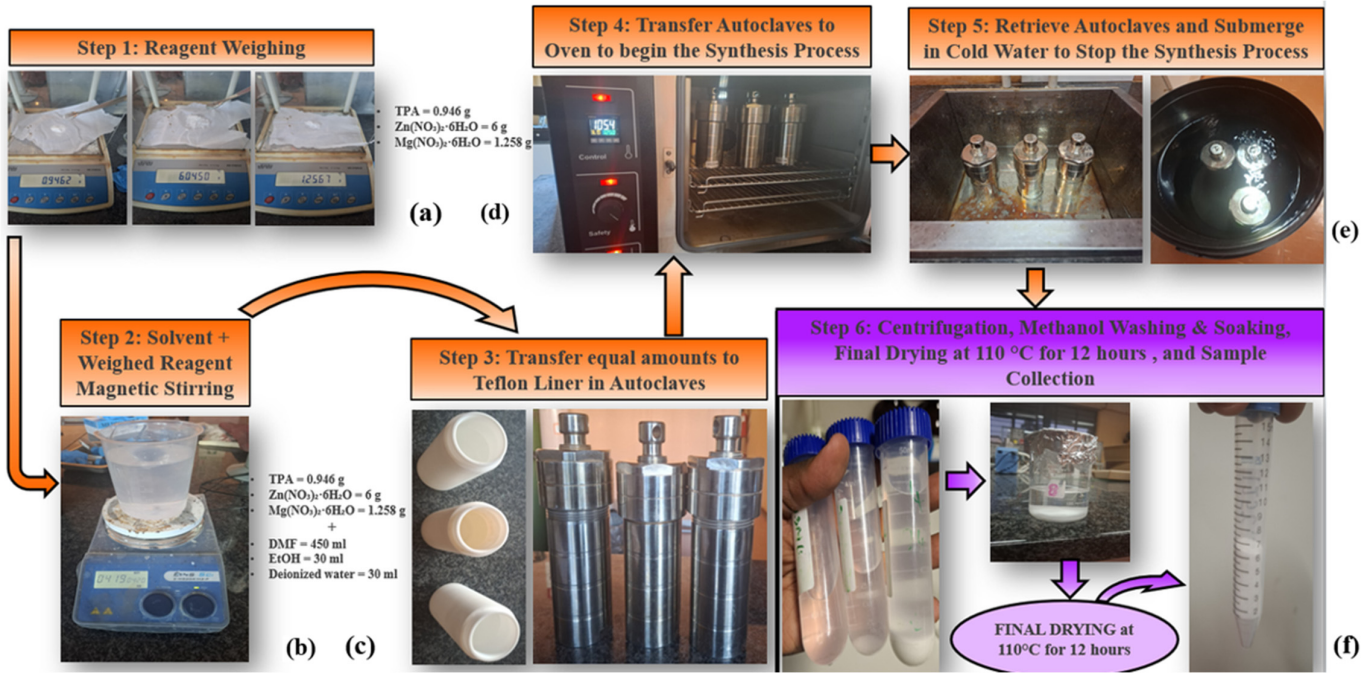


Figure 1. The flowchart for the synthesis of $Zn_{0.75}Mg_{0.25}$-MOF-74 showing (**a**) weighing of reagents; (**b**) magnetic stirring in the solvent mixture; (**c**) transfer into the autoclave Teflon liners; (**d**) solvothermal reaction in the oven; (**e**) cold-water quenching; and (**f**) centrifugation, methanol washing, and drying at 110 °C.

2.3. Characterization

Fourier Transform Infrared Spectroscopy (FTIR) was conducted using a PerkinElmer Spectrum Two spectrometer (PerkinElmer) equipped with an attenuated total reflectance (ATR) accessory, operating within the 4000–400 cm^{-1} range at a resolution of 4 cm^{-1}. The FTIR was used to identify functional groups and verify metal–ligand coordination within the synthesized frameworks. X-ray Diffraction (XRD) (Malvern PANalytical) was performed using a PANalytical X'Pert PRO diffractometer fitted with Cu Kα radiation (λ = 1.5406 Å), operated at 40 kV and 40 mA, scanning over a 2θ range of 5–50° with a step size of 0.02°. XRD was used to examine the crystallinity, phase purity, and structural topology of the synthesized MOFs. Scanning Electron Microscopy coupled with Energy Dispersive X-ray Spectroscopy (SEM-EDS) (ZEISS) was conducted using a ZEISS EVO MA10 scanning electron microscope equipped with an Oxford Instruments EDS detector. SEM-EDS was used to investigate the surface morphology, particle size, and elemental composition of the synthesized MOFs [38]. The SEM imaging provided information on particle shape, uniformity, and aggregation tendencies, while EDS mapping verified the framework elemental composition. Brunauer–Emmett–Teller (BET) (Micromeritics) surface area and porosity analyses were conducted using a Micromeritics TriStar II Plus instrument with nitrogen adsorption–desorption isotherms recorded at 77 K. Approximately 1 g of each sample was degassed under vacuum at 150 °C for 12 h to remove physiosorbed gases and moisture prior to analysis. The BET equation was applied within the relative pressure range of 0.05–0.30, and pore-size distributions were derived from the Barrett–Joyner–Halenda (BJH) and t-Plot models. This technique was essential for determining surface area, total pore volume, and pore-size distribution, thereby providing quantitative insight into the textural characteristics of the Zn/Mg-MOF-74 materials [39]. Direct CO_2 adsorption analysis was performed on the 125 °C, 30 h sample at the South African Council for Scientific and Industrial Research (CSIR) using a Micromeritics ASAP 2020 instrument with CO_2 as the adsorbate, an analysis bath temperature of 293 K (20 °C), and pressures

up to ~1 bar. This measurement was undertaken to provide a direct, application-relevant assessment of the bimetallic framework's CO_2 capture capability and to probe the ultramicroporosity not accessible to N_2 at 77 K.

3. Results

3.1. Surface Chemistry (Fourier Transform Infrared Spectroscopy—FTIR)

The FTIR analysis was conducted to verify the successful coordination of the organic linker with Zn^{2+} and Mg^{2+} nodes during the synthesis of the bimetallic Zn/Mg-MOF-74 and to identify the functional groups associated with framework formation. The technique was used to identify the unique vibrational signatures of carboxylate, hydroxyl, and metal–oxygen bonds that define the MOF-74 structure, while also allowing for a comparison of samples synthesized under different temperatures and reaction times to evaluate how these parameters affect the integrity of the structure and bond formation. In this study, terephthalic acid (TPA) was used instead of 2,5-dihydroxyterephthalic acid (DHTP) to determine whether MOF-74 could still form in the absence of additional hydroxyl coordination sites, as it was successfully used in a separate study by Gonçalves et al. [40] to form single metal MOFs of a different variation to MOF-74.

The main vibrational bands that verify the creation of the MOF-74 framework are indicated by vertical dashed lines in Figure 2. The hydroxyl (O-H) stretching vibrations are represented by broad absorption bands observed at 3500–3700 cm^{-1}, which are attributed to adsorbed water molecules or unreacted hydroxyl groups from the solution [41]. For the sample synthesized at 125 °C for 30 h, the relative strength of these bands reduced when compared to the sample synthesized by [13], indicating better framework dehydration and fewer trapped solvent molecules. The lower intensity is an indication of greater potential for the TPA synthesized MOFs to perform well in humid conditions [42]. Peaks appearing at approximately 1560 cm^{-1} and 1410 cm^{-1} represent the asymmetric and symmetric stretching vibrations of coordinated carboxylate (COO^-) groups, respectively [41]. The C=O band at approximately 1560 cm^{-1} confirms the coordination of terephthalate ligands with the Zn^{2+} and Mg^{2+} metal centres [43]. The band at approximately 1410 cm^{-1} is mainly attributed to C-O stretching, validating successful incorporation of the TPA ligand into the framework [43]. The strong carboxylate–metal interactions in the MOF-74 structure are indicated by the presence of these paired bands as well as their moderate strength and narrowness [13]. The enhanced coordination stability and reduced surface hydroxylation improve the availability of open metal sites, which are the primary adsorption centres for CO_2 molecules. Taken together, the FTIR results support two conclusions. First, the paired asymmetric and symmetric COO^- stretches at approximately 1560 and 1410 cm^{-1} confirm that terephthalate coordinates to the Zn^{2+} and Mg^{2+} centres through its carboxylate oxygens, so assembly of the MOF-74 framework proceeds without the additional hydroxyl coordination sites of 2,5-dihydroxyterephthalic acid. Second, the carboxylate and metal–oxygen bands report on linker coordination rather than on the identity of the metal centre and are consequently insensitive to the Zn:Mg ratio: the 125 °C, 5 h sample, which contains 0.30 at% magnesium, is not distinguishable on this basis from the 125 °C, 30 h sample at 11.39 at%. FTIR therefore establishes that coordination has occurred but not which metal has been incorporated, and composition was determined independently by EDS (Table 1).

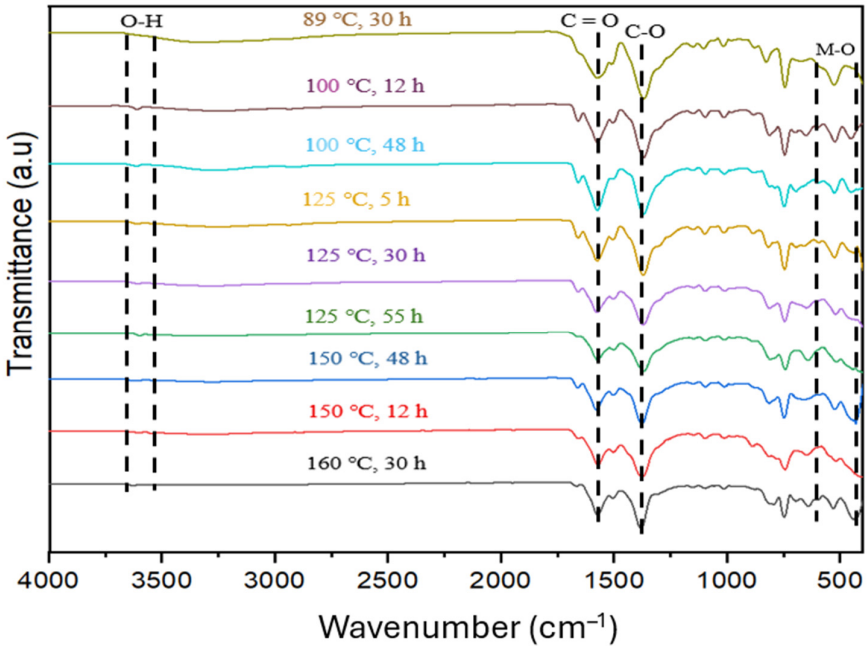


Figure 2. FTIR spectra of bimetallic $Zn_{0.75}Mg_{0.25}$-MOF-74 samples synthesized at varying reaction temperatures and time.

3.2. Crystallinity (X-Ray Diffraction—XRD)

The characteristic diffraction peaks of the MOF-74 framework are observed within the 2θ range of 5–50° in Figure 3, confirming successful crystallization of the bimetallic structure [44]. Prominent reflections appear at 2θ values of approximately 7.7°, 8.9°, 10.9°, 17.7°, 28.8°, 32.9°, 38.1°, and 44.3°, each corresponding to the crystallographic planes (110), (210), (300), (430), (640), (750), (1000), and (1110) of the hexagonal MOF-74 structure, respectively [45,46]. These planes represent periodic stacking of the one-dimensional metal–oxygen chains bridged by terephthalate linkers, producing the characteristic rod-packed topology of MOF-74. The strongest reflection, observed at 2θ = 7.78° in every sample, corresponds to an interplanar spacing of d = 11.37 Å, and the two next most intense reflections at 2θ = 8.90° and 10.98° correspond to d = 9.94 Å and 8.06 Å, respectively. The sharp peaks at low angles (especially those at 7.7° and 8.9°) represent the fingerprint region of the framework and indicate the long-range order of the hexagonal channels [20]. Samples synthesized at 100 °C for 48 h, 125 °C for 5 h, and 125 °C for 30 h, displayed strong reflections in both the low-angle and mid-angle regions, confirming the presence of well-ordered, highly crystalline frameworks.

In contrast, the sample prepared at 89 °C, 30 h exhibited weakened and excessively broadened peaks, suggesting incomplete crystallization likely due to insufficient thermal energy for full coordination of the metal and linker precursors [20]. Samples produced at 150–160 °C showed weakened intensity and partial disappearance of mid-angle reflections (17.7° and 28.8°), indicating that the frameworks undergo structural collapse and amorphization resulting from linker decomposition beyond the thermal stability limit of MOF-74 [47].

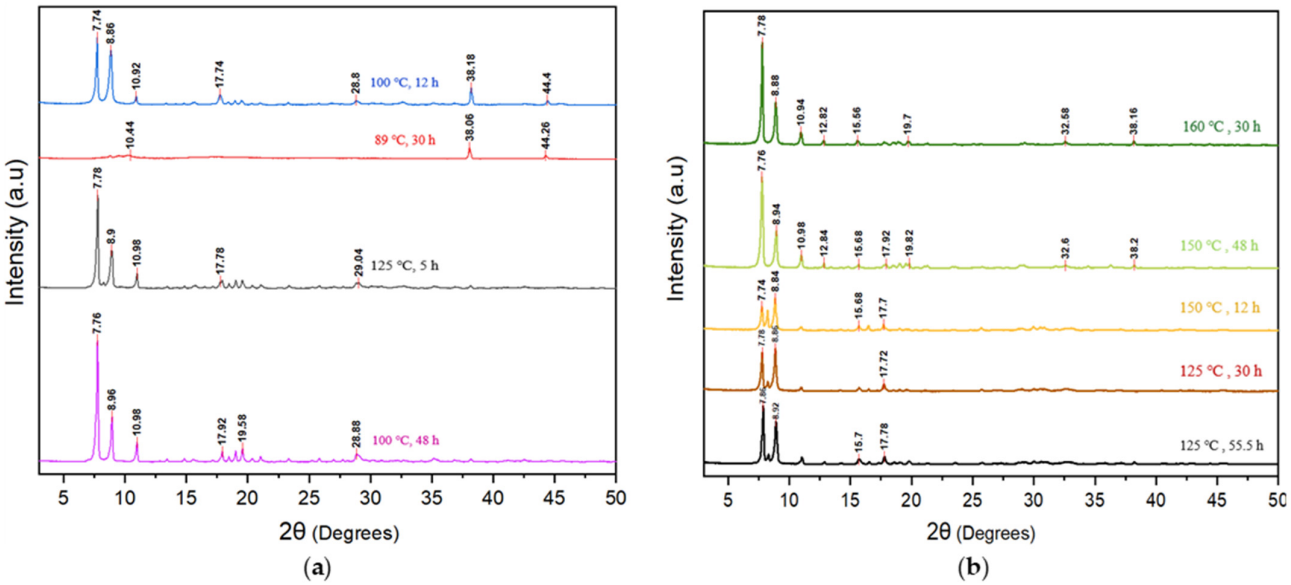


Figure 3. XRD spectra of bimetallic $Zn_{0.75}Mg_{0.25}$-MOF-74 samples synthesized at (**a**) four varying reaction temperatures and time; (**b**) five varying temperatures and reaction times.

3.3. Surface Morphology (SEM)

The SEM micrographs in Figure 4 illustrate the correlation of reaction time and synthesis temperature on crystal development, particle uniformity, and surface topographical characteristics. Sample (g), synthesized at 125 °C for 5 h, displayed uniform, well-defined rod-shaped crystals and minimal agglomeration. These long, hexagonal rods indicate successful and controlled crystal nucleation and fit the one-dimensional channel structure characteristic of MOF-74 [45]. The smooth surfaces and consistent rod shapes of these samples indicate a high degree of crystallinity and a well-developed external surface. Crystal habit of this kind reflects the geometry of nucleation and growth and governs the length of the diffusion path into the interior of each crystal. It does not, however, establish that the internal channel structure is fully formed since micropore development depends on the completeness of metal–linker coordination rather than on the outward shape the crystal adopts. Due to their high aspect ratio and well-organized packing, elongated hexagonal rods have the advantage of exposing a larger number of pore openings along the crystal surface, which promotes rapid gas penetration and shorter diffusion routes into the interior channels [45]. Such elongated rods reduce the likelihood of pore-blocking and shorten the transport path to the interior channels, but these are transport advantages rather than capacity advantages: they affect how readily CO_2 reaches adsorption sites, not how many such sites the framework contains. As Sections 3.4 and 3.5 show, sample (g) proved to be magnesium deficient despite this morphology, and CO_2 adsorption on it therefore does not represent the bimetallic system.

Notably, in contrast to other material prepared at low temperatures like (f) and (h), which were dominated by amorphous or reprecipitated particles, sample (i) at 100 °C for 12 h also had well-formed rod-shaped crystals. This indicates that considerable structural order was preserved by limiting over-growth and avoiding dissolution–reprecipitation effects through shorter exposure at a temperature less than 125 °C. Sample (i)'s rods are more homogeneous and less fractured than those of the other low-temperature samples in the 100 µm micrograph, indicating that ordered crystal growth was achieved under these conditions. This did not translate into adsorption capability. The EDS data in Figure 5 show a combined Zn + Mg content of only 7.66 at% for this sample against 63.76 at% carbon, while

Section 3.5 reports a t-plot micropore area of 0.04 m^2/g, identifying it as a predominantly mesoporous solid containing substantial unreacted linker despite its ordered external form.

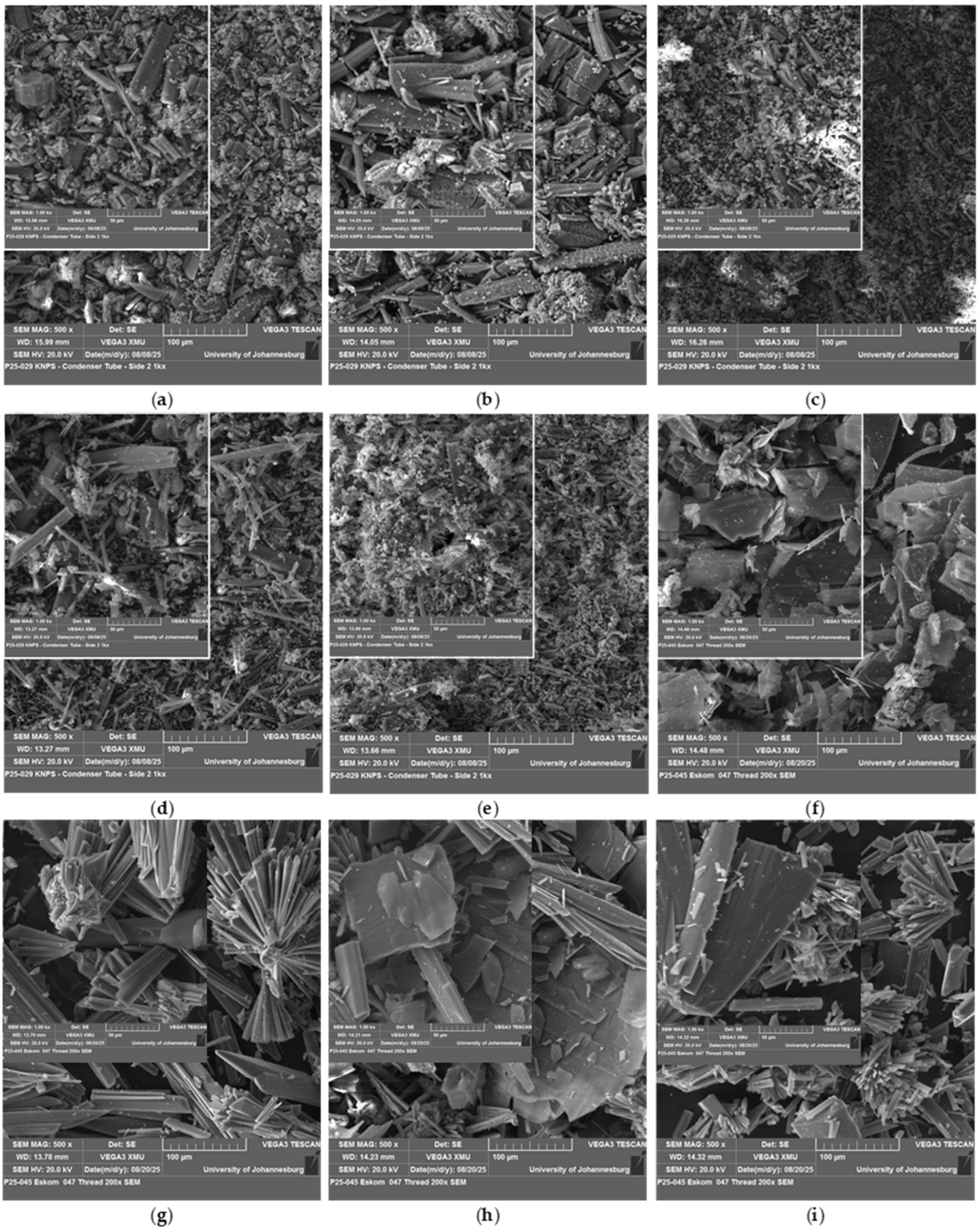


Figure 4. SEM micrographs at 100 µm and 20 µm for (**a**) 125 °C, 55.5 h; (**b**) 125 °C, 30 h; (**c**) 150 °C, 12 h; (**d**) 150 °C, 48 h; (**e**) 160 °C, 30 h; (**f**) 100 °C, 48 h; (**g**) 125 °C, 5 h; (**h**) 89 °C, 30 h; (**i**) 100 °C, 12 h.

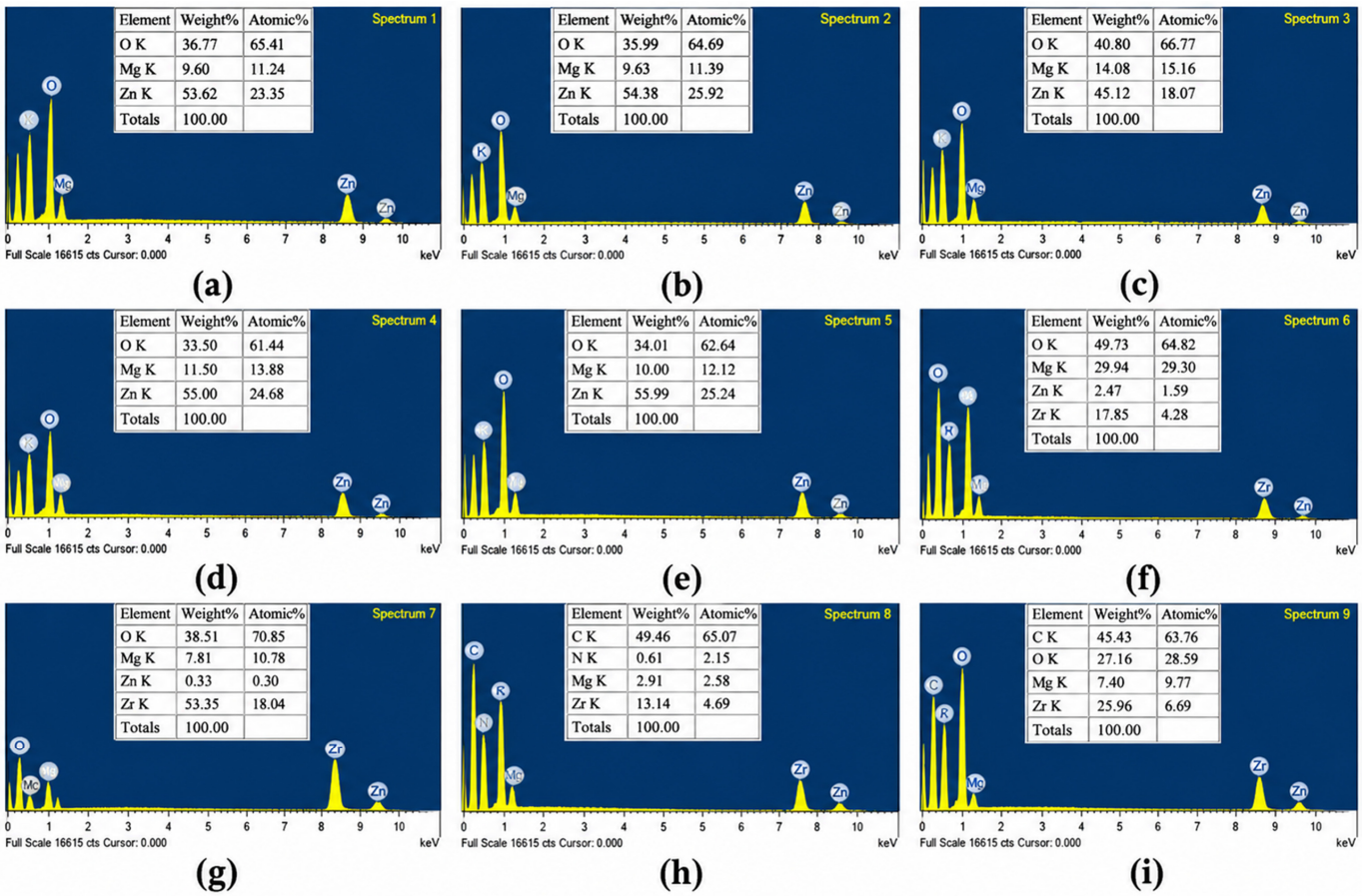


Figure 5. EDS of bimetallic $Zn_{0.75}Mg_{0.25}$-MOF-74 samples synthesized at (**a**) 125 °C, 55.5 h; (**b**) 125 °C, 30 h; (**c**) 150 °C, 12 h; (**d**) 150 °C, 48 h; (**e**) 160 °C, 30 h; (**f**) 100 °C, 48 h; (**g**) 125 °C, 5 h; (**h**) 89 °C, 30 h; (**i**) 100 °C, 12 h.

Samples (h) and (f), synthesized at lower temperatures and longer periods, i.e., 89 °C for 30 h and 100 °C for 48 h, respectively, show mixed and poorly defined morphologies with aggregated or partially dissolved crystals. These characteristics indicate incomplete coordination and reprecipitation during prolonged reaction at lower thermal energy. The irregular surfaces and compact agglomerates reduce pore accessibility and impede gas transport, which would negatively impact CO_2 uptake efficiency [48]. Samples (c), (d), and (e), synthesized at higher temperatures, i.e., 150–160 °C, had extensive amorphization and fused crystal structures, suggesting that the thermal stability limit of the organic linker was exceeded. This led to bond breakage and linker degradation, resulting in the collapse of the porous framework. Such structural collapse drastically decreases the internal surface area and reduces the number of accessible adsorption sites [48]. As a result, these high-temperature samples were expected to exhibit poor CO_2 adsorption performance in spite of potentially higher yields, as excessive crystal coalescence blocks the microchannels critical for gas diffusion. Overall, the SEM micrographs establish that well-ordered rod-like morphology is obtained under moderate synthesis conditions around 125 °C and is lost both below and above that window. Morphology alone, however, proved a poor predictor of adsorption performance in this system. The two samples with the most sharply defined rods, (g) and (i), were subsequently found to be respectively magnesium-deficient and effectively non-microporous, while sample (b), which the micrographs do not distinguish as exceptional, carried the microporous fraction that governs low-pressure CO_2 capture. Rod-like habit is therefore treated here as a necessary but not sufficient indicator of framework

quality, with composition and probe-accessible porosity established independently in the sections that follow.

3.4. Elemental Composition (EDS)

Figure 5 confirmed the presence of Zn, Mg, and O as the primary elements of the bimetallic $Zn_{0.75}Mg_{0.25}$-MOF-74 structure. The relative abundance of Zn remained consistently higher than Mg in all samples, in line with the targeted Zn-rich formulation and the stronger coordination affinity of Zn^{2+} toward the terephthalate linker [43]. Sample (b), synthesized at 125 °C for 30 h, displayed a Zn:Mg atomic ratio of approximately 0.68:0.32. As Table 1 shows, this was the closest approach to the targeted $Zn_{0.75}Mg_{0.25}$ stoichiometry among the well-coordinated frameworks, taken here as those with a combined Zn + Mg content above 30 at%. Samples (f) and (h) return nominally closer ratios of 0.73:0.27 and 0.76:0.24, but their combined metal contents are only 5.87 and 6.19 at%, so these ratios derive from weak signals in material that XRD and SEM show to be poorly crystallized and do not represent framework stoichiometry. The near-target ratio in sample (b) indicates that both metals had sufficient time to coordinate uniformly into the inorganic nodes during the solvothermal reaction. This balanced incorporation is critical because it introduces dual Lewis acidic sites with slightly different electronegativities, which collectively strengthen CO_2 binding through simultaneous interactions with the oxygen and carbon atoms of the adsorbate [13].

In contrast, sample (g), synthesized at 125 °C for only 5 h, displayed a markedly different elemental profile dominated by C (70.88 at%) and Zn (18.04 at%) with a Mg signal of just 0.30 at%, indicating that the short reaction time was insufficient for magnesium successful incorporation into the framework. This kinetic outcome is consistent with the slower coordination behaviour of Mg^{2+} relative to Zn^{2+} in solvothermal systems [23,43]. The high carbon signal in sample (g) further suggests the presence of unreacted or weakly bound terephthalate linker entrapped within the partially formed framework, which the 5 h reaction time was insufficient to fully integrate. While sample (g) consequently retained the favourable rod-like crystallinity observed by SEM, the resulting framework was effectively a Zn-MOF-74 variant rather than the targeted bimetallic $Zn_{0.75}Mg_{0.25}$-MOF-74. It therefore lies outside the compositional scope of this study and forfeits the bimetallic synergy that motivates the use of mixed Zn^{2+}/Mg^{2+} centres. Although direct CO_2 adsorption measurement of sample (g) gave a higher uptake (0.381 mmol/g) than the targeted 125 °C, 30 h bimetallic sample (0.310 mmol/g), it was excluded from further consideration on compositional grounds: as an essentially monometallic Zn-MOF-74 framework, its adsorption behaviour does not represent the bimetallic Zn/Mg-MOF-74 system that is the subject of this study.

Samples (c), (d), and (e), synthesized in the range of 150–160 °C, exhibited reduced Mg incorporation and elevated Zn dominance, suggesting partial Mg volatilization or phase segregation at elevated temperatures, conditions that reduce active site diversity and weaken CO_2 affinity. Samples (f), (h), and (i) displayed pronounced C and N peaks, attributed to residual terephthalate linker and DMF solvent molecules entrapped within the pores due to incomplete framework formation at insufficient thermal energy. Overall, the EDS results confirm that sample (b) at 125 °C for 30 h produced the most chemically homogeneous bimetallic framework matching the target stoichiometry, with both Zn^{2+} and Mg^{2+} incorporated into the metal–oxygen nodes at close to the intended ratio.

Table 1. The EDS elemental composition (atomic %) and normalized Zn:Mg ratios of the $Zn_{0.75}Mg_{0.25}$-MOF-74 samples synthesized under the nine reaction conditions.

Sample	Synthesis Conditions	C	O	Mg	Zn	Zn + Mg	Zn:Mg
(a)	125 °C, 55.5 h	-	65.41	11.24	23.35	34.59	0.68:0.32
(b)	125 °C, 30 h	-	64.69	11.39	23.92	35.31	0.68:0.32
(c)	150 °C, 12 h	-	66.77	15.16	18.07	33.23	0.54:0.46
(d)	150 °C, 48 h	-	61.44	13.88	24.68	38.56	0.64:0.36
(e)	160 °C, 30 h	-	62.64	12.12	25.24	37.36	0.68:0.32
(f)	100 °C, 48 h	64.82	29.30	1.59	4.28	5.87	0.73:0.27
(g)	125 °C, 5 h	70.88	10.78	0.30	18.04	18.34	0.98:0.02
(h)	89 °C, 30 h	65.07	26.58	1.50	4.69	6.19	0.76:0.24
(i)	100 °C, 12 h	63.76	28.59	0.97	6.69	7.66	0.87:0.13

Values are atomic percentages read from the EDS spectra in Figure 5; "-" denotes not detected. Sample (h) additionally contained 2.15 at% N, attributed to residual DMF retained within the pores. Zn:Mg ratios are normalized so that Zn + Mg = 1.

3.5. Textural Properties (N_2-LPGA)

Nine $Zn_{0.75}Mg_{0.25}$-MOF-74 samples were synthesized; however, only those prepared at 100 °C for 12 h and 125 °C for 30 h underwent the textural properties analysis using the low-pressure gas adsorption (LPGA) technique with N_2 as the adsorbate. Sample selection was guided by the combined evidence from XRD (Figure 3), SEM (Figure 4), and EDS (Figure 5), each of which had to support the existence of a well-coordinated bimetallic $Zn_{0.75}Mg_{0.25}$-MOF-74 framework before further characterization. The two chosen samples had relatively consistent rod-shaped morphology, well-ordered crystalline structure, and no nitrogenous impurities occupying possible adsorption sites as shown in Figure 5 and were on this basis selected for textural analysis.

Table 2 shows that synthesis temperature and duration have a strong influence on the pore structure of the bimetallic framework. The 100 °C, 12 h sample exhibited a higher BET surface area of 18.56 m^2/g and total pore volume of 0.0505 cm^3/g, but this surface area was dominated almost entirely by external mesopores (t-plot external area = 18.52 m^2/g out of 18.56 m^2/g total). The framework was effectively mesoporous, with negligible micropore content (t-plot micropore area = 0.04 m^2/g). In the context of CO_2 capture from flue gas where CO_2 partial pressures are typically 0.10–0.15 bar, mesoporous surfaces are weak adsorbers because the energy of adsorption on open surfaces is too low to retain CO_2 at sub-atmospheric partial pressure [49]. Strong CO_2 capture under these conditions requires confined micropores in which overlapping van der Waals potentials from opposing pore walls produce enhanced adsorption energies [25]. The 100 °C, 12 h sample lacked this characteristic.

Table 2. N_2 BET data for the selected synthesized $Zn_{0.75}Mg_{0.25}$-MOF-74 variants.

Synthesis Temp. and Time	BET Surface Area (m^2/g)	t-Plot Micropore Area (m^2/g)	t-Plot External Area (m^2/g)	Total Pore Volume (cm^3/g)	Average Pore Diameter (Å)	HK Median Pore Width (nm)	Particle Size (nm)
100 °C, 12 h	18.56	0.04	18.52	0.0505	109	1.04	323.2
125 °C, 30 h	11.26	3.11	8.15	0.0393	133	1.07	532.9

The 125 °C, 30 h sample, by contrast, exhibited the pore structure associated with strong low-pressure CO_2 capture. Its relatively lower overall BET surface area of 11.26 m^2/g was overshadowed by a t-plot micropore area of 3.11 m^2/g, which was higher than that of the 100 °C, 12 h sample, and a Horváth–Kawazoe (H-K) median pore width of 1.07 nm. The H-K median pore widths of both samples confirmed the existence of micropores in

the sub-2 nm range characteristic of MOF-74 channels [30]. Within these channels, CO_2 molecules encounter overlapping van der Waals potentials from opposing pore walls, leading to enhanced adsorption at low pressures and higher adsorption energies [25]. The t-plot micropore area of the 125 °C, 30 h sample is approximately 77 times greater than the 100 °C, 12 h sample (3.11 vs. 0.04 m^2/g).

The N_2 adsorption–desorption isotherms in Figure 6 show that the 100 °C, 12 h sample adsorbed significantly more N_2 than the 125 °C, 30 h sample across the entire relative pressure range. Both isotherms displayed a Type IV(a) shape with an H3 hysteresis loop, confirming mesoporous behaviour typical of slit-like channels [50]. The negative Langmuir surface areas recorded for both samples are similarly non-physical and resulted from the breakdown of the Langmuir monolayer model under multilayer adsorption conditions rather than from framework failure. The higher N_2 uptake of the 100 °C, 12 h sample reflected its larger external mesoporous surface, on which N_2 condenses readily at 77 K. It was not, however, an indicator of superior CO_2 capture. At 77 K, N_2 molecules lack sufficient thermal energy to diffuse efficiently through sub-1 nm channels. As a result, a framework with dense, narrow micropores can appear to under-perform a more open mesoporous one in N_2 measurements, even though its pores are readily accessible to CO_2 at near-ambient temperatures. This was confirmed directly through the CO_2 adsorption analysis presented in Section 3.6, which demonstrates the 125 °C, 30 h sample's ultra-micropores are accessible to CO_2 at 293 K despite their inaccessibility to N_2 at 77 K.

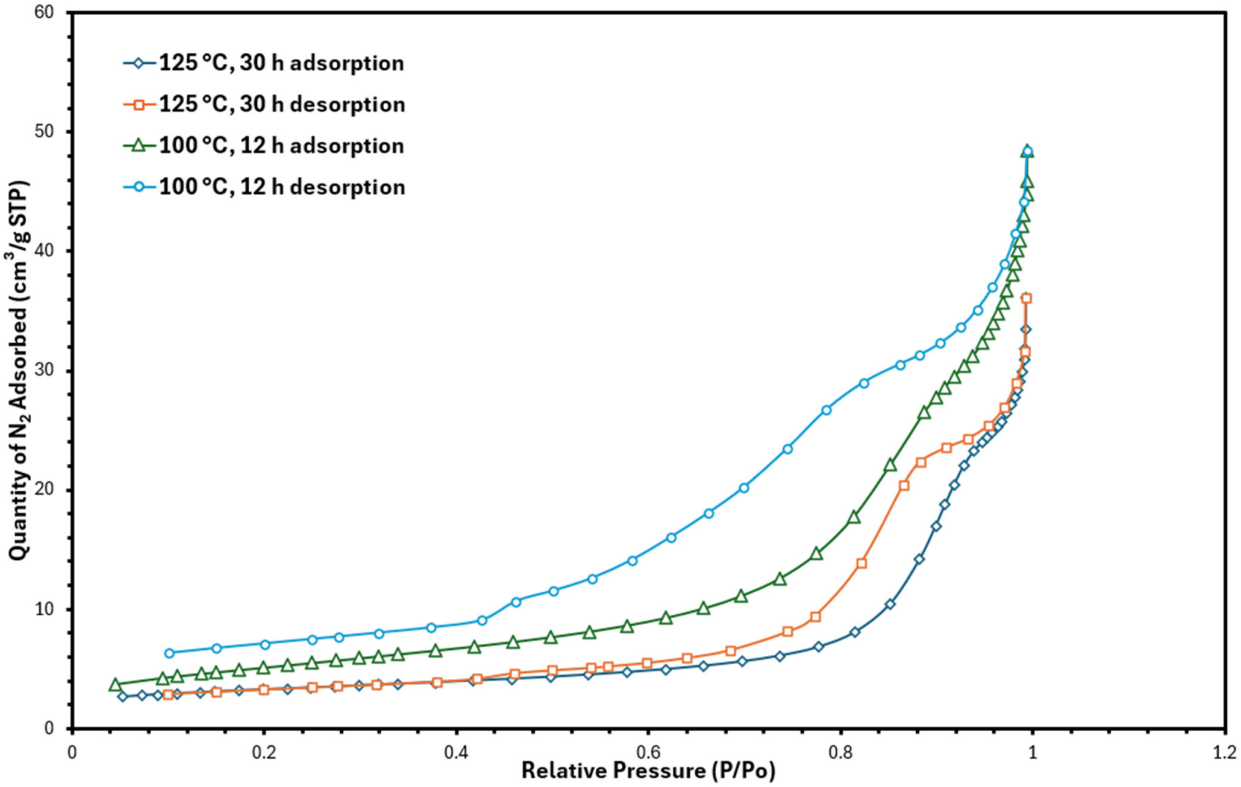


Figure 6. The N_2 adsorption and desorption isotherms for samples synthesized at 100 °C, 12 h and 125 °C, 30 h.

Overall, the N_2-LPGA results showed that the two samples are texturally distinct. The 100 °C, 12 h sample is dominated by external mesoporous surface area, while the 125 °C, 30 h sample is characterized by a smaller but well-developed microporous fraction with the well-defined channel structure of MOF-74. For CO_2 capture under flue-gas conditions where CO_2 partial pressures are sub-atmospheric and selectivity over N_2 depends on

micropore confinement, the 125 °C, 30 h sample is the more application relevant of the two frameworks.

3.6. CO_2 Adsorption Performance

The CO_2 adsorption isotherm in Figure 7, measured at 293 K, showed a smooth, concave-down contour that rose sharply at low pressures and curved toward a plateau at higher pressures. This was indicative of a Type I isotherm in the IUPAC classification, which is characteristic of micropore-dominated adsorption in which CO_2 molecules fill narrow channels through strengthened van der Waals interactions with opposing pore walls [50]. The absence of hysteresis-related features confirmed that adsorption proceeded entirely through micropore filling rather than capillary condensation, consistent with the rod-packed one-dimensional channel topology of MOF-74 indicated by XRD and SEM.

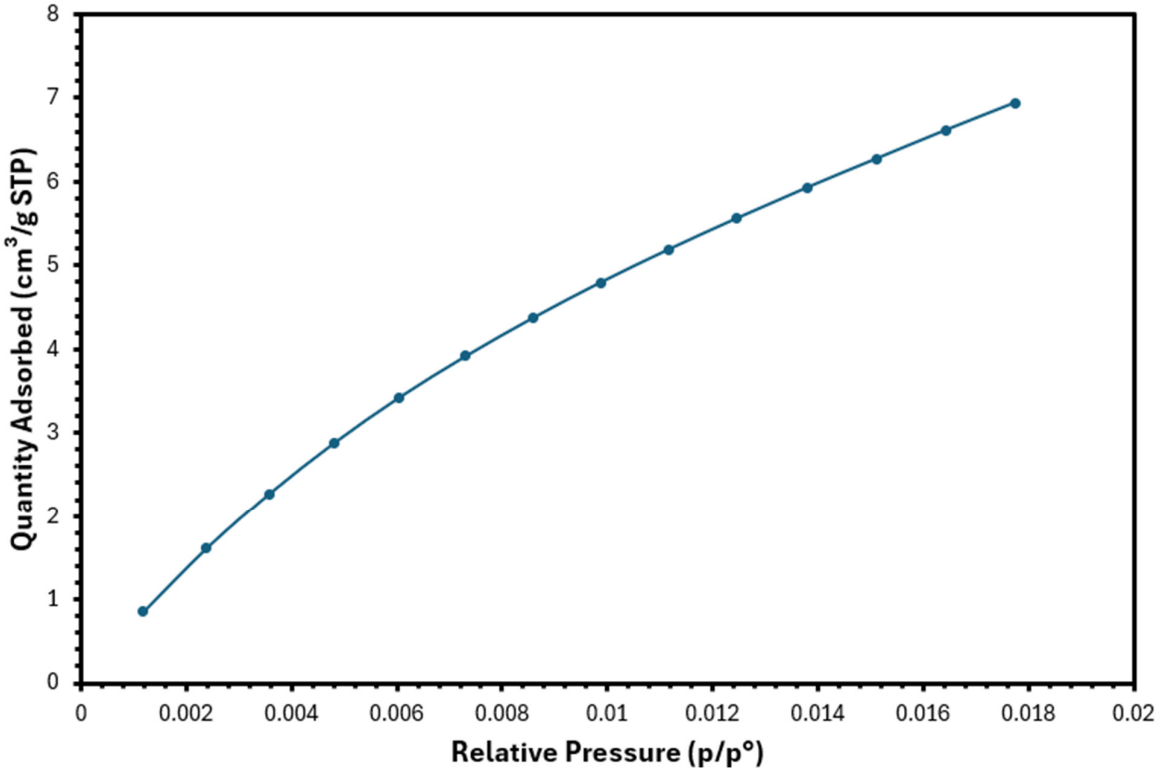


Figure 7. The CO_2 adsorption isotherm of the 125 °C, 30 h sample at 293 K (≤1 bar). The surface area and micropore parameters were derived by applying the BET, Langmuir, and Dubinin–Astakhov models to the CO_2 isotherm.

The CO_2-derived surface area of 60.10 m^2/g was more than five times higher than the N_2-derived BET value of 11.26 m^2/g obtained for the same sample in Table 2. This disparity was consistent with the kinetic restriction of N_2 at 77 K within sub-1 nm channels. At cryogenic temperatures, N_2 molecules lack the thermal energy to diffuse efficiently into ultra-micropores, leading to an under-estimation of accessible surface area [50]. CO_2 at 293 K, with significantly higher thermal energy and a smaller kinetic diameter (3.30 Å versus 3.64 Å for N_2), penetrates these channels easily. The Langmuir surface area of 63.46 m^2/g obtained from the CO_2 isotherm fitted with a correlation coefficient of 0.999 in contrast to the non-physical negative Langmuir values returned by the N_2 measurement. The close agreement between the BET and Langmuir surface areas (60.10 and 63.46 m^2/g) and the high quality of the Langmuir fit supported a single-monolayer adsorption mechanism within well-defined micropores at the pressures investigated.

The full set of CO_2 adsorption parameters is summarized in Table 3. The Dubinin–Astakhov (D-A) analysis, which is calibrated for CO_2 adsorption in microporous materials, returned a micropore surface area of 131.69 m^2/g and a limiting micropore volume of 0.0409 cm^3/g. These values further confirmed the presence of a substantial ultramicroporous fraction in the framework and provided a more accurate textural description than the t-plot approach, which is calibrated against N_2 at 77 K standard isotherms and is therefore inappropriate for CO_2 probe data [25]. The Dubinin–Radushkevich (D-R) monolayer capacity of 22.1 cm^3/g STP exceeded the experimental uptake at 1 bar by a factor of approximately three, indicating that the framework retained substantial spare capacity that would be realized at the higher pressures encountered in pre-combustion CO_2 capture or in pressurized flue-gas processes.

Table 3. CO_2 adsorption parameters for the 125 °C, 30 h $Zn_{0.75}Mg_{0.25}$-MOF-74 sample at 293 K.

Parameter	Value
CO_2 uptake at ~1 bar, cm^3/g STP (mmol/g)	6.94 (0.310)
CO_2 uptake at ~0.135 bar (flue-gas-relevant), cm^3/g STP (mmol/g)	1.61 (0.072)
Working pressure range (14 isotherm points), mbar	67–1016
BET surface area (R = 0.9987), m^2/g	60.10
Langmuir surface area (R = 0.9984), m^2/g	63.46
Langmuir monolayer capacity (Q_m), cm^3/g STP	13.89
Langmuir affinity constant (b), $mbar^{-1}$	9.50×10^{-4}
Dubinin–Astakhov micropore surface area (R = 0.99999), m^2/g	131.69
Dubinin–Astakhov limiting micropore volume, cm^3/g	0.0409
Dubinin–Radushkevich micropore surface area, m^2/g	100.99
Dubinin–Radushkevich monolayer capacity, cm^3/g STP	22.11

The CO_2 uptake at ~1 bar reached 6.94 cm^3/g STP, equivalent to 0.31 mmol/g. At a flue-gas-relevant partial pressure of ~0.135 bar, the uptake was 1.61 cm^3/g STP (0.072 mmol/g).

4. Discussion

4.1. Framework Formation with Terephthalic Acid

The working hypothesis of this study was that terephthalic acid (TPA) could substitute for 2,5-dihydroxyterephthalic acid (2,5-DHTP) as the organic linker in bimetallic Zn/Mg-MOF-74 without preventing framework formation. The results support this hypothesis. FTIR confirmed carboxylate–metal coordination through the paired asymmetric and symmetric COO^- bands, and XRD reproduced the characteristic low-angle reflections of the hexagonal MOF-74 topology, demonstrating that the two carboxylate groups of TPA are sufficient to assemble the rod-packed one-dimensional channel structure in the absence of the hydroxyl coordination sites present in 2,5-DHTP (Figure 8). This extends the earlier observation that TPA forms stable single-metal frameworks [40] to the bimetallic Zn/Mg-MOF-74 system, which has previously been reported only with 2,5-DHTP [13,20]. The reduced intensity of the O-H stretching bands relative to the 2,5-DHTP-derived material of [13] is consistent with the lower framework polarity expected of a linker without hydroxyl substituents and suggests reduced hydrophilicity, the property that has been identified as the principal cause of moisture-induced degradation in MOF-74 [30,31].

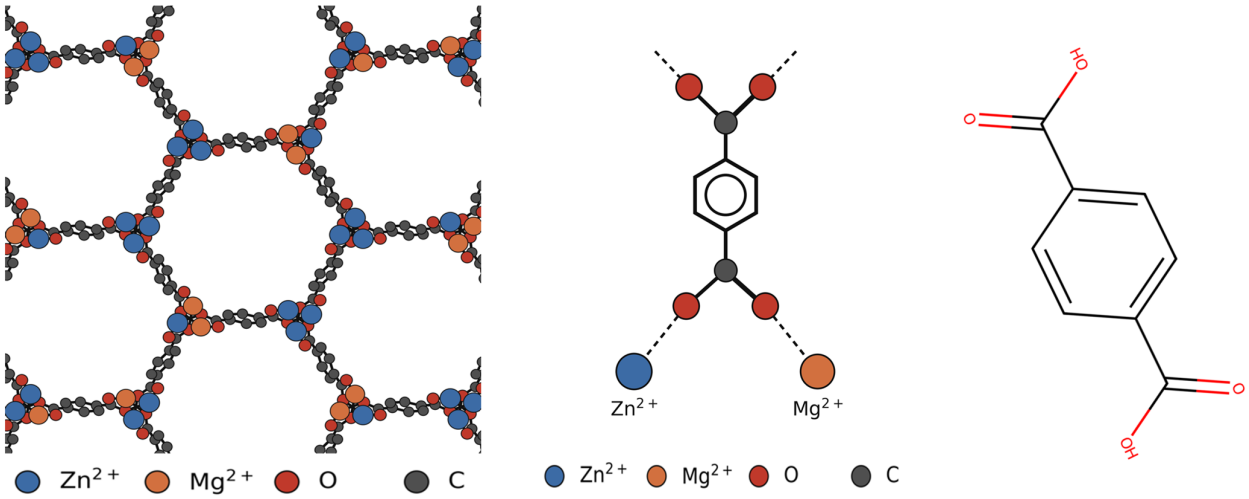


Figure 8. The proposed structure of terephthalate-linked $Zn_{0.75}Mg_{0.25}$-MOF-74: (**a**) the framework along the channel axis; (**b**) carboxylate bridging between Zn^{2+} and Mg^{2+} centres; (**c**) terephthalic acid linker. Hydrogen atoms omitted.

4.2. Effect of Synthesis Conditions

Synthesis reaction temperature and time jointly governed framework quality, and the results define a narrow processing window. Below this window, at 89 °C, insufficient thermal energy left crystallization incomplete, producing broadened XRD reflections and poorly defined morphology. Above it, at 150–160 °C, the loss of mid-angle reflections and the extensive amorphization observed by SEM indicate that the thermal stability limit of the linker was exceeded, consistent with reports of linker decomposition and framework collapse in MOF-74 at elevated temperature [47,49]. Reaction time proved equally decisive, and its effect was compositional rather than purely structural. The EDS profile of the 5 h sample, in which magnesium was essentially absent, shows that Zn^{2+} and Mg^{2+} do not coordinate on the same timescale: the slower incorporation of Mg^{2+} relative to Zn^{2+} [23,43] means that a short reaction yields a Zn-dominated framework that, whatever its crystallinity, forfeits the dual Lewis acidic sites that motivate the bimetallic design [13]. Only at 125 °C over 30 h did both metals incorporate at a Zn:Mg ratio approaching the target stoichiometry. Framework quality in this system therefore cannot be inferred from crystallinity alone; composition must be verified independently.

The two metals are included for different reasons. Mg^{2+} carries the higher charge density and forms the stronger Lewis acid–base interaction with CO_2, which is what raises uptake at low partial pressure in Mg-MOF-74 [19,23]. Zn^{2+} forms Zn-O bonds that resist hydrolysis, the failure mode that limits Mg-MOF-74 in humid gas [19,21,24]. The Zn-rich 0.75:0.25 ratio weights the framework towards stability on the reasoning that capacity can be recovered through linker chemistry whereas framework collapse cannot. Whether that balance is right for a terephthalate-linked framework is addressed in Section 4.5.

4.3. Probe-Dependent Porosity and CO_2 Accessibility

The divergence between the N_2 and CO_2 measurements is the central textural finding of this study and warrants careful interpretation. Judged on N_2 adsorption at 77 K alone, the 100 °C, 12 h sample would appear the superior adsorbent, with a higher BET surface area and greater total pore volume. That conclusion would be mistaken. Its surface area is almost entirely external and mesoporous, and mesoporous surfaces are weak CO_2 adsorbers at the sub-atmospheric partial pressures characteristic of flue gas, where adsorption depends on

the enhanced potentials generated within confined micropores [25,50]. The 125 °C, 30 h sample, despite a lower N_2-derived surface area, carries the micropore fraction that matters. Direct CO_2 measurement at 293 K confirmed this: the CO_2-derived BET surface area of 60.10 m^2/g and the Dubinin–Astakhov micropore surface area of 131.69 m^2/g exceed the N_2-derived value of 11.26 m^2/g several times over. The discrepancy is kinetic in origin, as N_2 at 77 K lacks the thermal energy to access sub-1 nm channels that CO_2, with a smaller kinetic diameter and higher thermal energy at 293 K, enters readily [50]. The practical implication extends beyond this material: N_2 physisorption at 77 K, the default textural characterization for porous adsorbents, can systematically understate the CO_2-accessible porosity of ultra-microporous frameworks. Screening MOF-74 analogues for carbon capture based on N_2-derived surface area alone therefore risks discarding the better adsorbent.

4.4. Adsorption Performance in the Context of Previous Studies

The measured uptake of 0.31 mmol/g at ~1 bar and 0.072 mmol/g at flue-gas-relevant conditions is substantially below the 4–8 mmol/g reported for 2,5-DHTP-derived Zn/Mg-MOF-74 and its single-metal counterparts [13,19,22]. This shortfall is neither unexpected nor indicative of a defective synthesis; it is the predicted consequence of the linker substitution. The hydroxyl groups of 2,5-DHTP occupy positions adjacent to the carboxylate and generate open Lewis basic sites that strongly polarize the CO_2 quadrupole, driving the high adsorption affinity for which MOF-74 is known [20,30]. TPA offers no such groups, yielding a framework that is structurally analogous but chemically less affinity rich. The Type I isotherm and the absence of hysteresis nevertheless confirm that adsorption proceeds by micropore filling within the MOF-74 channels rather than by surface condensation, so the capture mechanism is preserved even as the capacity is reduced. The Dubinin–Radushkevich monolayer capacity of 22.1 cm^3/g STP, roughly three times the uptake measured at 1 bar, further indicates that the framework retains unused capacity that would be accessed at the elevated pressures of pre-combustion or pressurized flue-gas capture.

4.5. Implications and Future Work

The significance of this result lies in what is exchanged for the reduced capacity. On a mass basis 2,5-DHTP costs roughly six times more than TPA [32], and its reactive hydroxyl groups and multi-step synthesis make it sensitive to solvent, pH, and temperature variation, complicating scale-up [33]. A linker that is inexpensive, commercially abundant, and synthetically robust addresses the cost barrier that has kept MOF-74 from industrial deployment [29]. Whether the trade-off is favourable cannot be settled by equilibrium capacity alone: the relevant metric for a capture technology is cost per tonne of CO_2 captured over the operating lifetime of the adsorbent, which depends jointly on capacity, regeneration energy, and stability under repeated cycling in humid gas. The intermediate binding energy of bimetallic Zn/Mg frameworks [25] and the reduced hydrophilicity implied by the FTIR results are both favourable on the latter two counts, but neither was measured directly here, and this is the principal limitation of the present work.

Four routes could raise capacity without giving up the cost advantage of the TPA linker. The first is composition. The Zn:Mg ratio used here was taken from 2,5-DHTP frameworks, and terephthalate frameworks may have a different optimum: magnesium's advantage depends on an exposed Mg^{2+} centre, and the phenolate oxygens that help expose it are absent here. A Zn:Mg series at 125 °C for 30 h would locate it. The second is linker chemistry. Replacing a small fraction of the TPA with 2,5-DHTP, or with an amino-substituted terephthalate, would add Lewis basic sites while keeping most of the framework cheap. Affinity and cost then trade continuously rather than as a binary choice. The third is activation. These samples were dried at 110 °C and degassed at 150 °C; solvent

exchange followed by longer vacuum activation would clear residual solvent and unreacted linker, recovering pore volume that is occupied rather than absent. The fourth is pressure. The Dubinin–Radushkevich monolayer capacity of 22.11 cm^3/g STP is roughly three times the uptake measured at 1 bar, so much of the capacity is available at the higher pressures of pre-combustion or pressurized flue-gas capture.

Adsorption–desorption cycling should be performed to establish capacity retention and regenerability over repeated cycles. Secondly, the isosteric heat of adsorption should be determined to quantify the regeneration energy penalty and test whether the intermediate binding energy predicted for Zn/Mg systems is realized with a TPA linker. Furthermore, performance should be assessed under humid, mixed-gas conditions representative of industrial flue gas, which is where the projected moisture stability of the TPA framework would translate into a practical advantage over 2,5-DHTP-derived analogues. Lastly, the capacity routes outlined above should be tested experimentally. Establishing that TPA yields a functional bimetallic MOF-74 framework, as this study has done, is a precondition for that work rather than an endpoint.

5. Conclusions

The aim of this study was to synthesize bimetallic $Zn_{0.75}Mg_{0.25}$-MOF-74 using terephthalic acid (TPA) as an alternative organic linker and evaluate its physicochemical properties for CO_2 capture. The framework was successfully synthesized via a solvothermal method, with FTIR confirming metal–ligand coordination, XRD verifying MOF-74 crystallinity, and SEM-EDS showing well-defined rod-like morphology under optimal conditions. BET analysis showed that the 100 °C, 12 h sample exhibited a higher surface area (18.56 m^2/g) and total pore volume (0.0505 cm^3/g), indicating dominant mesoporosity, while the 125 °C, 30 h sample showed a lower surface area (11.26 m^2/g) but a far larger micropore area (3.11 m^2/g against 0.04 m^2/g), consistent with confined adsorption sites. N_2 adsorption indicated higher uptake for the 100 °C, 12 h sample; however, this behaviour was attributed to external mesoporous surface area rather than enhanced CO_2 adsorption performance. CO_2 adsorption analysis at 293 K confirmed that the 125 °C, 30 h sample contained accessible ultra-micropores not detected by N_2 at 77 K, with a CO_2-derived BET surface area of 60.10 m^2/g and a Dubinin–Astakhov micropore surface area of 131.69 m^2/g. The Type I isotherm and uptake of 0.31 mmol/g at ~1 bar (0.072 mmol/g at ~0.135 bar) confirm micropore-dominated adsorption behaviour. Although substantially lower than the 4–8 mmol/g reported for 2,5-DHTP-based Zn/Mg-MOF-74 systems, this reduced uptake reflects the absence of hydroxyl functional groups in TPA and represents a predictable trade-off between adsorption affinity and improved cost, scalability, and potential moisture stability. Further work should focus on evaluating adsorption–desorption cycling stability, determining the heat of adsorption, and assessing performance under mixed-gas conditions representative of flue gas. In conclusion, $Zn_{0.75}Mg_{0.25}$-MOF-74 can be successfully synthesized using TPA, producing a crystalline and microporous framework with confirmed CO_2 adsorption capability. Synthesis at 125 °C for 30 h yields the best-balanced material. It combines the target Zn:Mg stoichiometry with a developed microporous fraction and validated CO_2 adsorption performance. Shorter reaction times at this temperature give magnesium-deficient frameworks, and lower temperatures give ordered crystals without micropore development.

Author Contributions: Conceptualization, S.B.N., G.M., and M.M.; methodology, S.B.N., G.M., D.B., T.M., and M.M.; investigation, S.B.N.; resources, T.M. and M.M.; writing, original draft preparation, S.B.N.; writing, review and editing, S.B.N., G.M., D.B., T.M., and M.M.; supervision, G.M. and M.M. All authors have read and agreed to the published version of the manuscript.

Funding: This study was funded by National Research Foundation (NRF), grant number TTK250322305772.

Institutional Review Board Statement: Not applicable.

Informed Consent Statement: Not applicable.

Data Availability Statement: The data presented in this study are available on request from the corresponding author.

Acknowledgments: The authors would like to acknowledge the National Research Foundation for the funding. The University of Johannesburg is also acknowledged for its resources and research facilities.

Conflicts of Interest: The authors declare no conflicts of interest. The funders had no role in the design of the study; in the collection, analyses, or interpretation of data; in the writing of the manuscript; or in the decision to publish the results.

References

1. Cho, H.H.; Strezov, V. A Comparative Review on the Environmental Impacts of Combustion-Based Electricity Generation Technologies. *Energy Fuels* **2020**, *34*, 10486–10502. [CrossRef]
2. Dunmade, I.; Madushele, N.; Adedeji, P.A.; Akinlabi, E.T. A Streamlined Life Cycle Assessment of a Coal-Fired Power Plant: The South African Case Study. *Environ. Sci. Pollut. Res.* **2019**, *26*, 18484–18492. [CrossRef] [PubMed]
3. International Energy Agency. *CO_2 Emissions from Fuel Combustion: Highlights 2023*; IEA: Paris, France, 2023. Available online: https://www.iea.org/reports/co2-emissions-from-fuel-combustion-2023 (accessed on 12 July 2026).
4. Worldometer. CO_2 Emissions per Capita. Available online: https://www.worldometers.info/co2-emissions/co2-emissions-per-capita/ (accessed on 12 July 2026).
5. Nel, E.; Marais, L.; Mqotyana, Z. The Regional Implications of Just Transition in the World's Most Coal-Dependent Economy: The Case of Mpumalanga, South Africa. *Front. Sustain. Cities* **2023**, *4*, 1059312. [CrossRef]
6. Yoro, K.; Sekoai, P. The Potential of CO_2 Capture and Storage Technology in South Africa's Coal-Fired Thermal Power Plants. *Environments* **2016**, *3*, 24. [CrossRef]
7. Liang, Z.; Fu, K.; Idem, R.; Tontiwachwuthikul, P. Review on Current Advances, Future Challenges and Consideration Issues for Post-Combustion CO_2 Capture Using Amine-Based Absorbents. *Chin. J. Chem. Eng.* **2016**, *24*, 278–288. [CrossRef]
8. Shen, M.; Tong, L.; Yin, S.; Liu, C.; Wang, L.; Feng, W.; Ding, Y. Cryogenic Technology Progress for CO_2 Capture under Carbon Neutrality Goals: A Review. *Sep. Purif. Technol.* **2022**, *299*, 121734. [CrossRef]
9. Drenchev, N.L.; Shivachev, B.L.; Dimitrov, L.D.; Hadjiivanov, K.I. Effect of Water on CO_2 Adsorption on CaNaY Zeolite: Formation of $Ca^{2+}(H_2O)(CO_2)$, $Ca^{2+}(H_2O)(CO_2)_2$ and $Ca^{2+}(H_2O)_2(CO_2)$ Complexes. *Nanomaterials* **2023**, *13*, 2278. [CrossRef] [PubMed]
10. Inthawong, S.; Wongkoblap, A.; Intomya, W.; Tangsathitkulchai, C. The Enhancement of CO_2 and CH_4 Capture on Activated Carbon with Different Degrees of Burn-Off and Surface Chemistry. *Molecules* **2023**, *28*, 5433. [CrossRef] [PubMed]
11. Adeniyi, A.G.; Iwuozor, K.O.; Emenike, E.C.; Sagboye, P.A.; Micheal, K.T.; Micheal, T.T.; Saliu, O.D.; James, R. Biomass-Derived Activated Carbon Monoliths: A Review of Production Routes, Performance, and Commercialization Potential. *J. Clean. Prod.* **2023**, *423*, 138711. [CrossRef]
12. Ding, L.; Xu, N.; Wu, Y.; Li, P.; Bai, J.; Hai, W.; Li, R.; Yang, Y.; Liu, J.; Gao, C.-Y. Exploring the Performance Improvement for CO_2 Chemical Fixation in Zn/ZnMg-MOFs. *Inorg. Chem.* **2024**, *63*, 3317–3326. [CrossRef] [PubMed]
13. Gao, Z.; Liang, L.; Zhang, X.; Xu, P.; Sun, J. Facile One-Pot Synthesis of Zn/Mg-MOF-74 with Unsaturated Coordination Metal Centers for Efficient CO_2 Adsorption and Conversion to Cyclic Carbonates. *ACS Appl. Mater. Interfaces* **2021**, *13*, 61334–61345. [CrossRef] [PubMed]
14. Jiao, L.; Seow, J.Y.R.; Skinner, W.S.; Wang, Z.U.; Jiang, H.-L. Metal-Organic Frameworks: Structures and Functional Applications. *Mater. Today* **2019**, *27*, 43–68. [CrossRef]
15. Fan, R.; Kang, N.; Li, Y.; Gao, L. A Template-Directed Synthesis of Metal-Organic Framework (MOF-74) Ultrathin Nanosheets for Oxygen Reduction Electrocatalysis. *RSC Adv.* **2021**, *11*, 9353–9360. [CrossRef] [PubMed]
16. Britt, D.; Furukawa, H.; Wang, B.; Glover, T.G.; Yaghi, O.M. Highly Efficient Separation of Carbon Dioxide by a Metal-Organic Framework Replete with Open Metal Sites. *Proc. Natl. Acad. Sci. USA* **2009**, *106*, 20637–20640. [CrossRef] [PubMed]
17. Yang, X.; Wang, Q.; Chen, J.; Liu, H.; Xu, L.; Rao, M. Competitive Adsorption of Moisture and SO_2 for Carbon Dioxide Capture by Zeolites FAU 13X and LTA 5A. *Processes* **2024**, *12*, 1547. [CrossRef]
18. Abdeljaoued, A.; Querejeta, N.; Durán, I.; Álvarez-Gutiérrez, N.; Pevida, C.; Chahbani, M.H. Preparation and Evaluation of a Coconut Shell-Based Activated Carbon for CO_2/CH_4 Separation. *Energies* **2018**, *11*, 1748. [CrossRef]

19. Kari, N.E.F.; Bustam, M.A.; Ismail, M. Metal-Organic Frameworks: Screening M-MOF-74 (M = Co, Cr, Cu, Fe, Mg, Mn, Ni, Ti, and Zn) Based for Carbon Dioxide Adsorption. *E3S Web Conf.* **2021**, *287*, 02011. [CrossRef]
20. Beamish-Cook, J.; Shankland, K.; Murray, C.A.; Vaqueiro, P. Insights into the Mechanochemical Synthesis of MOF-74. *Cryst. Growth Des.* **2021**, *21*, 3047–3055. [CrossRef] [PubMed]
21. Voskanyan, A.A.; Goncharov, V.G.; Novendra, N.; Guo, X.; Navrotsky, A. Thermodynamics Drives the Stability of the MOF-74 Family in Water. *ACS Omega* **2020**, *5*, 13158–13163. [CrossRef] [PubMed]
22. Adhikari, A.K.; Lin, K.-S. Synthesis, Fine Structural Characterization, and CO_2 Adsorption Capacity of Metal Organic Frameworks-74. *J. Nanosci. Nanotechnol.* **2014**, *14*, 2709–2717. [CrossRef] [PubMed]
23. Wauteraerts, N.; Tu, M.; Chanut, N.; Rodríguez-Hermida, S.; Gandara-Loe, J.; Ameloot, R. Vapor-Assisted Synthesis of the MOF-74 Metal-Organic Framework Family from Zinc, Cobalt, and Magnesium Oxides. *Dalton Trans.* **2023**, *52*, 17873–17880. [CrossRef] [PubMed]
24. Xin, C.; Hou, S.; Yu, L.; Zhou, X.; Fu, Y.; Yang, X.; Sun, W.; Yang, F.; Wang, X.; Liu, L. Controlled Synthesis of Mg-MOF-74 and Its CO_2 Adsorption in Flue Gas. *Coatings* **2024**, *14*, 383. [CrossRef]
25. Maia, R.A.; Louis, B.; Gao, W.; Wang, Q. CO_2 Adsorption Mechanisms on MOFs: A Case Study of Open Metal Sites, Ultra-Microporosity and Flexible Framework. *React. Chem. Eng.* **2021**, *6*, 1118–1133. [CrossRef]
26. Mahreni; Ristianingsih, Y. A Review on Metal-Organic Framework (MOF): Synthesis and Solid Catalyst Applications. *Yogyakarta Conf. Ser. Proc. Eng. Sci. Ser.* **2020**, *11*, 638–645.
27. Forsyth, C.; Taras, T.; Johnson, A.; Zagari, J.; Collado, C.; Hoffmann, M.M.; Reed, C.R. Microwave Assisted Surfactant-Thermal Synthesis of Metal-Organic Framework Materials. *Appl. Sci.* **2020**, *10*, 4563. [CrossRef]
28. Bose, S.; Sengupta, D.; Malliakas, C.D.; Idrees, K.B.; Xie, H.; Wang, X.; Barsoum, M.L.; Barker, N.M.; Dravid, V.P.; Islamoglu, T.; et al. Suitability of a Diamine Functionalized Metal-Organic Framework for Direct Air Capture. *Chem. Sci.* **2023**, *14*, 9380–9388. [CrossRef] [PubMed]
29. Hui, Q.; Fu, J.; Xu, H.; Wang, C.; Ding, Q.; Zhu, W.; Sun, J.; Zhou, Z.; Wu, Y.; Hu, X.; et al. Metal-Organic Frameworks for CO_2 Capture: Challenges and Efforts from Laboratory Research to Industrial Applications. *Ind. Eng. Chem. Res.* **2025**, *64*, 9457–9483. [CrossRef]
30. Xin, C.; Ren, Y.; Zhang, Z.; Liu, L.; Wang, X.; Yang, J. Enhancement of Hydrothermal Stability and CO_2 Adsorption of Mg-MOF-74/MCF Composites. *ACS Omega* **2021**, *6*, 7739–7745. [CrossRef] [PubMed]
31. An, Y.; Lv, X.; Jiang, W.; Wang, L.; Shi, Y.; Hang, X.; Pang, H. The Stability of MOFs in Aqueous Solutions-Research Progress and Prospects. *Green Chem. Eng.* **2024**, *5*, 187–204. [CrossRef]
32. Calpac Laboratory. Chemical and Laboratory Supplies. Available online: https://www.calpaclab.com/ (accessed on 12 July 2026).
33. Yusuf, V.F.; Malek, N.I.; Kailasa, S.K. Review on Metal-Organic Framework Classification, Synthetic Approaches, and Influencing Factors: Applications in Energy, Drug Delivery, and Wastewater Treatment. *ACS Omega* **2022**, *7*, 44507–44531. [CrossRef] [PubMed]
34. Luttrell, W.E.; Hester, R.L. Terephthalic Acid. *J. Chem. Health Saf.* **2016**, *23*, 49–52. [CrossRef]
35. Xiao, C.; Tian, J.; Chen, Q.; Hong, M. Water-Stable Metal-Organic Frameworks (MOFs): Rational Construction and Carbon Dioxide Capture. *Chem. Sci.* **2024**, *15*, 1570–1610. [CrossRef] [PubMed]
36. Liu, X.; Wang, X.; Kapteijn, F. Water and Metal-Organic Frameworks: From Interaction toward Utilization. *Chem. Rev.* **2020**, *120*, 8303–8377. [CrossRef] [PubMed]
37. Pang, L.; Lei, Y.; Zou, Y.; Yu, F.; Feng, F.; Lu, J.; Kong Pang, W.; Liu, Z.; Liu, P.; O'Mullane, A.P.; et al. Revealing the Effects of Functional Group in Organic Linkers on Properties of Metal Organic Frameworks Electrode and Their Performance in Supercapacitors. *Chem. Eng. J.* **2024**, *500*, 157470. [CrossRef]
38. Dourandish, Z.; Tajik, S.; Beitollahi, H.; Jahani, P.M.; Nejad, F.G.; Sheikhshoaie, I.; Di Bartolomeo, A. A Comprehensive Review of Metal-Organic Framework: Synthesis, Characterization, and Investigation of Their Application in Electrochemical Biosensors for Biomedical Analysis. *Sensors* **2022**, *22*, 2238. [CrossRef] [PubMed]
39. Zheng, A.; Yin, K.; Pan, R.; Zhu, M.; Xiong, Y.; Sun, L. Research Progress on Metal-Organic Frameworks by Advanced Transmission Electron Microscopy. *Nanomaterials* **2023**, *13*, 1742. [CrossRef] [PubMed]
40. Gonçalves, J.M.R.; Brandao, J.V.; Neto, B.S.L. A Synthesis of Metal-Organic Frameworks Using Terephthalic Acid Obtained from PET Bottles with Dye Adsorption for Application in Experimental Chemistry Classes. *Discov. Chem.* **2025**, *2*, 144. [CrossRef]
41. Hadjiivanov, K.I.; Panayotov, D.A.; Mihaylov, M.Y.; Ivanova, E.Z.; Chakarova, K.K.; Andonova, S.M.; Drenchev, N.L. Power of Infrared and Raman Spectroscopies to Characterize Metal-Organic Frameworks and Investigate Their Interaction with Guest Molecules. *Chem. Rev.* **2021**, *121*, 1286–1424. [CrossRef] [PubMed]
42. Jasuja, H.; Huang, Y.; Walton, K.S. Adjusting the Stability of Metal-Organic Frameworks under Humid Conditions by Ligand Functionalization. *Langmuir* **2012**, *28*, 16874–16880. [CrossRef] [PubMed]
43. Ling, J.; Zhou, A.; Wang, W.; Jia, X.; Ma, M.; Li, Y. One-Pot Method Synthesis of Bimetallic MgCu-MOF-74 and Its CO_2 Adsorption under Visible Light. *ACS Omega* **2022**, *7*, 19920–19929. [CrossRef] [PubMed]

44. Quintelier, M.; Hajizadeh, A.; Zintler, A.; Gonçalves, B.F.; Fernández De Luis, R.; Esrafili Dizaji, L.; Vande Velde, C.M.L.; Wuttke, S.; Hadermann, J. In Situ Study of the Activation Process of MOF-74 Using Three-Dimensional Electron Diffraction. *Chem. Mater.* **2024**, *36*, 7274–7282. [CrossRef] [PubMed]
45. Wu, C.; Chu, X.; Wu, X.; Zhou, H.; Zeng, Y.; Wang, D.; Liu, W. Size and Morphology Control over MOF-74 Crystals. *RSC Adv.* **2024**, *14*, 20604–20608. [CrossRef] [PubMed]
46. Liu, Z.; He, K.; Yang, Z.; Xu, Z.; Li, M.; Zhang, J.; Yao, C.; Chen, Q.; Li, X. Plasma-Induced Reconstruction of CoNi-MOF-74 into Nanoporous Surfaces at Room Temperature for Enhanced Oxygen Evolution Reaction. *ACS Appl. Nano Mater.* **2025**, *8*, 23016–23026. [CrossRef]
47. Healy, C.; Patil, K.M.; Wilson, B.H.; Hermanspahn, L.; Harvey-Reid, N.C.; Howard, B.I.; Kleinjan, C.; Kolien, J.; Payet, F.; Telfer, S.G.; et al. The Thermal Stability of Metal-Organic Frameworks. *Coord. Chem. Rev.* **2020**, *419*, 213388. [CrossRef]
48. Łuczak, J.; Kroczewska, M.; Baluk, M.; Sowik, J.; Mazierski, P.; Zaleska-Medynska, A. Morphology Control through the Synthesis of Metal-Organic Frameworks. *Adv. Colloid Interface Sci.* **2023**, *314*, 102864. [CrossRef] [PubMed]
49. Bui, M.; Adjiman, C.S.; Bardow, A.; Anthony, E.J.; Boston, A.; Brown, S.; Fennell, P.S.; Fuss, S.; Galindo, A.; Hackett, L.A.; et al. Carbon Capture and Storage (CCS): The Way Forward. *Energy Environ. Sci.* **2018**, *11*, 1062–1176. [CrossRef]
50. Schlumberger, C.; Thommes, M. Characterization of Hierarchically Ordered Porous Materials by Physisorption and Mercury Porosimetry-A Tutorial Review. *Adv. Mater. Interfaces* **2021**, *8*, 2002181. [CrossRef]

Disclaimer/Publisher's Note: The statements, opinions and data contained in all publications are solely those of the individual author(s) and contributor(s) and not of MDPI and/or the editor(s). MDPI and/or the editor(s) disclaim responsibility for any injury to people or property resulting from any ideas, methods, instructions or products referred to in the content.